Journal of Loss Prevention in the Process Industries 68 (2020) 104274

Contents lists available at ScienceDirect

Journal of Loss Prevention in the Process Industries

journal homepage: http://www.elsevier.com/locate/jlp

CFD simulations of dust dispersion in the 1 m^3 explosion vessel

Maria Portarapillo [a], Marco Trofa [a], Roberto Sanchirico [b], Almerinda Di Benedetto [a,*]

[a] Department of Chemical, Materials and Production Engineering, University of Naples Federico II Naples, 80125, Italy
[b] Institute for Researches on Combustion-CNR, Naples, 80125, Italy

ARTICLE INFO

Keywords:
CFD simulation
Dust dispersion
Siwek sphere
1 m^3 vessel

ABSTRACT

According to standard procedures, flammability and explosion parameters for dusts and dust mixtures are evaluated in 20 L and/or 1 m^3 vessels, with equivalent results provided a correct ignition delay time (60 ms in the 20 L vessel; 600 ms in the 1 m^3 vessel). In this work, CFD simulations of flow field and dust concentration distribution in the 1 m^3 spherical vessel are performed, and the results compared to the data previously obtained for the 20 L. It has been found that in the 1 m^3 vessel, the spatial distribution of the turbulent kinetic energy is lower and much more uniform. Concerning the dust distribution, as in the case of the 20 L, dust is mainly concentrated at the outer zones of the vortices generated inside the vessel. Furthermore, an incomplete feeding is attained, with most of the dust trapped in the perforated annular nozzle. Starting from the maps of dust concentration and turbulent kinetic energy, the deflagration index K_{St} is calculated in both vessels. In the conditions of the present work, the K_{St} is found to be 2.4 times higher in the 20 L than in the 1 m^3 vessel.

1. Introduction

In chemical processes, several accidents are imputable to explosions of flammable dusts, dust mixtures, and hybrid mixtures (Dust Safety Science, 2020). In order to characterize the sensitivity and the severity of explosion in case of ignition, the explosibility and flammability parameters assessment is required. Most of these parameters (minimum explosible concentration, MEC; limiting oxygen concentration, LOC; maximum explosion pressure, P_{max}; deflagration index, K_{St}) are evaluated in 20 L and/or 1 m^3 vessels, according to standard procedures (ASTM E1226-19, 2019; ASTM E1515-14, 1993; ASTM E2931-13, 2013; BS EN 14034-1, 2004; ISO, 6184–1:1985, 1985). The 20 L sphere came out of a systematic investigation of several combustible dusts in spherical shaped equipment to find the minimum volume for dust testing (Bartknecht, 1989; Siwek, 1988, 1977). Indeed, the test method described in ASTM E1226-19 for 20 L sphere provides a procedure for performing laboratory tests to evaluate deflagration parameters of dusts that can be correlated to those from the 1 m^3 vessel (ASTM E1226-19, 2019). The calibration and standardization procedures for a 20 L chamber aim at obtaining the same evaluation of the deflagration parameters in both vessels. These are normally performed varying the dispersion procedure (especially the ignition delay time).

Immediately after dispersion, turbulence builds up and starts decreasing. Consequently, the turbulence level at moment of ignition significantly depends on the ignition delay time t_d which is the delay between the onset of dust dispersion and the activation of the ignition source.

Therefore, for dust testing in 20 L sphere, the ignition delay time has been standardized to (60 ± 5) ms, at which the degree of turbulence should be comparable to that achieved in the 1 m^3 vessel at (600 ± 100) ms (ASTM E1226-19, 2019; BS EN 14034-1, 2004).

Over a few years, several dusts have been tested with both equipment and significant discrepancies have been found between the results obtained with the 20 L sphere and the 1 m^3 vessel. In particular, some dusts although weakly reactive in the 20 L sphere are totally not explosible in the 1 m^3 vessel (Cashdollar and Chatrathi, 1992; Di Benedetto et al., 2012; Going et al., 2000; Rodgers and Ural, 2011). Proust et al. (2007) demonstrated that dusts having a value of $K_{St} < 45$ bar m/s measured in the 20 L sphere might be not explosible in the 1 m^3 vessel (Proust et al., 2007). Most studies have ascribed this effect to an overdriving due to preheating/ignition phenomena leading to false positives in smaller explosion chambers (Cashdollar and Chatrathi, 1992; Di Benedetto et al., 2012; Going et al., 2000; Rodgers and Ural, 2011). Conversely, K_{St} values of metal dusts (iron, zinc, and aluminium) can be much more severe when measured in the 1 m^3 chamber compared to values found in the more commonly used 20 L sphere (Clouthier et al., 2019; Taveau et al., 2019, 2018). This increase in the larger vessel has been attributed to the effect of thermal radiation, which can be an order of magnitude

* Corresponding author.
E-mail address: almerinda.dibenedetto@unina.it (A. Di Benedetto).

https://doi.org/10.1016/j.jlp.2020.104274
Received 17 June 2020; Received in revised form 27 July 2020; Accepted 19 August 2020
Available online 23 August 2020

greater for metal dusts compared to common organic dusts (Taveau et al., 2019). For this reason, NFPA 68 recommends to measure the explosion severity of the most reactive metal dusts in a 1 m^3 chamber (NFPA, 2018).

As regards the maximum explosion pressure, P_{max} values obtained with the 20 L sphere are significantly and systematically below the ones determined in the 1 m^3 vessel (Proust et al., 2007). Actually, because of the cooling effect from the walls of the 20 L sphere and the pressure effect caused by the pyrotechnic ignitors, in ASTM E1226-19 standard some correction correlation are present (ASTM E1226-19, 2019). The reasons why this difference occurs are not known but may suggest different combustion regimes in both equipment (Proust et al., 2007).

Proust examined the two vessels by plotting the values of K_{St} obtained in the in the 20 L versus the values obtained in the 1 m^3 vessel. From this plot it appears that these estimations are of the same order of magnitude but they may be very different in value, eventually giving different dust classification (Proust et al., 2007). Therefore, the estimation of K_{St} with the 20 L sphere may be conservative (generally, for organic and weakly reactive dusts) or not (metal dusts), even if the expected preheating phenomena in the 20 L sphere, resulting in oversized or undersized prevention/protection safety measures respectively (Bartknecht, 1989).

On the other hand, it is well known that preignition turbulence may play a major role in affecting the explosion behaviour. As a result, the control of the turbulence level in both vessels is of primary importance (Cashdollar, 1996; Di Benedetto et al., 2012).

In addition to the turbulence level issue, both standard vessels must be capable of dispersing a fairly uniform dust cloud of solid particles for a reliable and repeatable estimation of safety parameters (ASTM E1226-19, 2019; ASTM E1515-14, 1993; ASTM E2931-13, 2013; BS EN 14034-1, 2004; ISO, 1985–1:1985, 1985). Di Benedetto et al. (2013) have shown that within the 20 L sphere, it is not possible to generate uniform dust dispersion and turbulence (Di Benedetto et al., 2013). In particular, the turbulence level and the dust particle distribution inside the 20 L sphere significantly depend on the dust size (Di Benedetto et al., 2010; Di Sarli et al., 2013; Russo et al., 2013), concentration (Di Sarli et al., 2014) and shape (Russo and Di Benedetto, 2013). Moreover, the dispersion of dust mixtures is strongly affected by both diameter and density of the pure dusts (Portarapillo et al., 2020).

In previous works, different authors measured the turbulence level inside the 20 L sphere (Dahoe et al., 2002; Pu et al., 1991; van der Wel et al., 1992) and the 1 m^3 spherical/cylindrical vessel (Hauert and Vogl, 1995; Zhen and Leuckel, 1996). Turbulence measurements were performed through hot wire or laser doppler anemometry in few points of the vessel, mainly positioned at the centre or close to the dispersion system. Collected data allowed the evaluation of the temporal values of the instantaneous velocity and of the root mean square velocity fluctuations only in the selected points.

Furthermore, some researchers investigated the effectiveness of dust dispersion in various test vessels using optical dust probes in the 20 L sphere (Kalejaiye, 2001; Kalejaiye et al., 2010) and in the 1 m^3 ISO vessel (Cashdollar and Chatrathi, 1992; Hauert and Vogl, 1995). The measuring principle is based on the attenuation by absorption and dispersion of the intensity of a light beam penetrating a cloud with solid particles. Kalejaiye et al. used optical dust probes to measure optical transmittance through the dust cloud at six locations within the 20 L sphere, with the two standard dispersion nozzles (rebound and perforated annular nozzles). They tested the dispersion of three different dusts, showing that the transmission data of the three dusts were significantly lower than those corresponding to the nominal value. They attributed this difference to the reduction in particle size that occurred during dispersion (Kalejaiye, 2001; Kalejaiye et al., 2010). Cashdollar and Chatrathi (1992) carried out comparisons between the uniformity of the dust cloud formed in the PRL 20 L chamber and Fike 1 m^3 test vessel, using the PRL optical dust probes. They observed that the 1 m^3 transmission data were somewhat lower than in the 20 L chamber at low dust concentrations. A possible explanation for this behaviour is an increased agglomeration in the 20 L chamber (Cashdollar and Chatrathi, 1992). Hauert and Vogl (1995) measured the dust concentration of maize starch (diameter 15 μm, density 1000 kg/m^3, nominal concentration 120 g/m^3) in the 1 m^3 vessel in 9 different locations. Results showed differences in the transmission data at the different points, indicating that the dust cloud is non-uniform. In particular, the highest values of dust concentration were found on the bottom of the vessel due to the sedimentation phenomenon (Hauert and Vogl, 1995).

Due to the possibility of measurement of turbulence level and dust concentration only in few points of the vessels, maps of velocity vectors, turbulence degree, and dust concentration cannot be derived from experimental analyses. Moreover, no simulation is available for 1 m^3 vessel which allows the quantification of these maps. The aim of this work is to develop a CFD model able to get insights into the fluid flow which is established inside the 1 m^3 vessel, when injecting either only air or dust-air mixtures, and to visualize the dust dispersion process. The simulation results of turbulent kinetic energy and dust concentration are compared to that simulated in the of 20 L sphere, to evidence similarities and differences.

2. Model description

2.1. The explosion equipment: 1 m^3 vessel and 20 L sphere

CFD simulations were run of the standard 1 m^3 vessel apparatus described in several standards (BS EN 14034-1, 2004; ISO, 1985–1:1985, 1985). The core of the test facility is the spherical or cylindrical stainless-steel explosion chamber (aspect ratio 1:1 ± 10%), shown in Fig. 1. The dust to be dispersed is charged into a dust container (spherical or cylindrical) having a volume of 5.4 L. The dust container has an outlet at the base, through which the dust leaves the container. This outlet is closed by a fast-acting valve activated by a blasting cap. The fast-acting valve is connected to the side of the explosion vessel. The connecting tube between the fast-acting valve and the dust disperser must be no longer than 350 mm. For dispersing the dust, a perforated annular nozzle is mounted inside the explosion vessel, concentric with its wall. The perforated annular nozzle, with an internal diameter of 21.7 mm, is fitted with 13 holes of 6 mm in diameter. The required amount of dust is placed in the dust container. The container is then pressurised to an overpressure of 20 bar while the 1 m^3 vessel is left at atmospheric pressure. The delay between the initiation of the dust dispersion and activation of the ignition source (through two chemical igniters each having an energy of 5 kJ) must be (600 ± 100) ms.

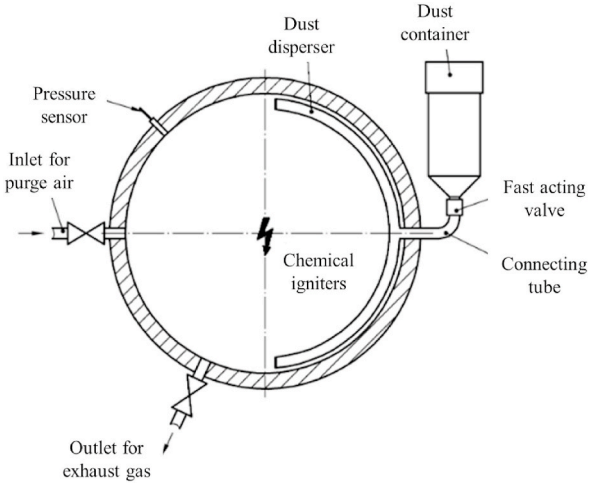

Fig. 1. *1 m^3 vessel for the determination of dust explosion parameters* (BS EN 14034-1, 2004).

CFD simulations of the standard 20 L sphere equipment, described in ASTM E1226-19 standard, were computed and the results are shown for the sake of comparison (ASTM E1226-19, 2019). The CFD model for this equipment was presented and used in previous studies (Di Benedetto et al., 2013; Di Sarli et al., 2015, 2014, 2013). In particular, we considered a 20 L sphere equipped with a rebound nozzle placed at the bottom side of the bomb. As reported in standard ASTM E1226-19, the rebound nozzle is an alternative to the perforated annular one for the formation of the dust cloud (ASTM E1226-19, 2019). Both nozzles should generate a uniform dust cloud within the spherical vessel. On the other hand, previous studies have shown that both dispersion systems have important issues and differences in the dust feed in the sphere, dust concentration distribution and turbulence level and control (Di Sarli et al., 2015). The objective of the test method described in ASTM E1226-19 is to produce data that can be correlated to those from the 1 m^3 vessel, whatever the nozzle used for the dust dispersion (ASTM E1226-19, 2019).

2.2. Model

The computational domain and mesh of 1 m^3 vessel were built and refined by means of the Design Modeler and Meshing packages of Ansys (Release 19). The sphere was modeled as three-dimensional and details of the annular ring nozzle were also reproduced. In addition, the container with the feeding tube of the dust was included in the computational domain (Fig. 2). The feeding tube length was set at the maximum allowable value (350 mm). In Table 1, geometrical details of the computational domain are given and in Fig. 3 a section of the unstructured and non-uniform mesh used is shown.

Full model description for 20 L sphere has been given in a previous paper (Di Benedetto et al., 2013). The model used for dispersion simulation in 1 m^3 vessel consists of the time-averaged Navier-Stokes equations (Eulerian approach), written in polar coordinates that read as follows (Eqs. (1)–(4)).

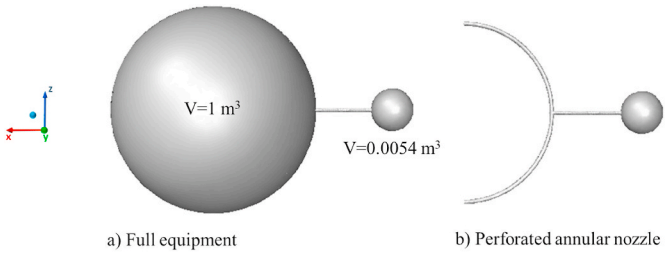

Fig. 2. Computational domain: full equipment (a) and perforated annular nozzle (b).

Table 1
Geometrical details of the computational domain.

Geometrical detail	Value
Container volume (m^3)	0.0054
Tube diameter (m)	0.02
Tube length (m)	0.35
Sphere volume (m^3)	1

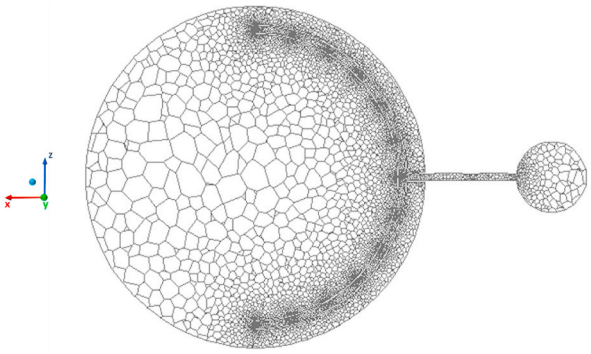

Fig. 3. Section of the unstructured and nonuniform mesh used, (x–z) central plane.

$$\frac{\partial \overline{\rho}}{\partial t}+\frac{1}{r^2}\frac{\partial\left(\overline{\rho} r^2 \overline{v}_r\right)}{\partial r}+\frac{1}{r sin\theta}\frac{\partial\left(\overline{\rho}\,\overline{v}_\theta sin\theta\right)}{\partial \theta}+\frac{1}{r sin\theta}\frac{\partial\left(\overline{\rho}\,\overline{v}_\varphi\right)}{\partial \varphi}=0 \tag{1}$$

$$\overline{\rho}\left(\frac{\partial \overline{v}_r}{\partial t}+\overline{v}_r\frac{\partial \overline{v}_r}{\partial r}+\frac{\overline{v}_\theta}{r}\frac{\partial \overline{v}_r}{\partial \theta}+\frac{\overline{v}_\varphi}{r sin\theta}\frac{\partial \overline{v}_r}{\partial \varphi}-\frac{\overline{v}_\theta{}^2+\overline{v}_\varphi{}^2}{r}\right)=-\frac{\partial p}{\partial r}-\left[\frac{1}{r^2}\frac{\partial}{\partial r}\left(r^2\overline{\tau}_{rr}{}^{(v)}\right)+\frac{1}{r sin\theta}\frac{\partial}{\partial \theta}\left(\overline{\tau}_{\theta r}^{(v)} sin\theta\right)+\frac{1}{r sin\theta}\frac{\partial}{\partial \varphi}\left(\overline{\tau}_{\varphi r}^{(v)}\right)-\frac{\overline{\tau}_{\theta\theta}^{(v)}+\overline{\tau}_{\varphi\varphi}^{(v)}}{r}\right]$$
$$-\left[\frac{1}{r^2}\frac{\partial}{\partial r}\left(r^2\overline{\tau}_{rr}{}^{(t)}\right)+\frac{1}{r sin\theta}\frac{\partial}{\partial \theta}\left(sin\theta\overline{\tau}_{\theta r}^{(t)}\right)+\frac{1}{r sin\theta}\frac{\partial}{\partial \varphi}\left(\overline{\tau}_{\varphi r}^{(t)}\right)-\frac{\overline{\tau}_{\theta\theta}^{(t)}+\overline{\tau}_{\varphi\varphi}^{(t)}}{r}\right]+\overline{\rho} g_r \tag{2}$$

$$\overline{\rho}\left(\frac{\partial \overline{v}_\theta}{\partial t}+\overline{v}_r\frac{\partial \overline{v}_\theta}{\partial r}+\frac{\overline{v}_\theta}{r}\frac{\partial \overline{v}_\theta}{\partial \theta}+\frac{\overline{v}_\varphi}{r sin\theta}\frac{\partial \overline{v}_\theta}{\partial \varphi}-\frac{\overline{v}_r\overline{v}_\theta-\overline{v}_\varphi{}^2 cot\theta}{r}\right)=-\frac{1}{r}\frac{\partial p}{\partial \theta}-\left[\frac{1}{r^3}\frac{\partial}{\partial r}\left(r^3\overline{\tau}_{r\theta}{}^{(v)}\right)+\frac{1}{r sin\theta}\frac{\partial}{\partial \theta}\left(\overline{\tau}_{\theta\theta}^{(v)} sin\theta\right)+\frac{1}{r sin\theta}\frac{\partial}{\partial \varphi}\left(\overline{\tau}_{\varphi\theta}^{(v)}\right)+\frac{\overline{\tau}_{\theta r}^{(v)}-\overline{\tau}_{r\theta}^{(v)}+\overline{\tau}_{\varphi\varphi}^{(v)} cot\theta}{r}\right]$$
$$-\left[\frac{1}{r^3}\frac{\partial}{\partial r}\left(r^3\overline{\tau}_{r\theta}{}^{(t)}\right)+\frac{1}{r sin\theta}\frac{\partial}{\partial \theta}\left(\overline{\tau}_{\theta\theta}^{(t)} sin\theta\right)+\frac{1}{r sin\theta}\frac{\partial}{\partial \varphi}\left(\overline{\tau}_{\varphi\theta}^{(t)}\right)+\frac{\overline{\tau}_{\theta r}^{(t)}-\overline{\tau}_{r\theta}^{(t)}+\overline{\tau}_{\varphi\varphi}^{(t)} cot\theta}{r}\right]+\overline{\rho} g_\theta \tag{3}$$

$$\overline{\rho}\left(\frac{\partial \overline{v}_\varphi}{\partial t}+\overline{v}_r\frac{\partial \overline{v}_\varphi}{\partial r}+\frac{\overline{v}_\theta}{r}\frac{\partial \overline{v}_\varphi}{\partial \theta}+\frac{\overline{v}_\varphi}{r sin\theta}\frac{\partial \overline{v}_\varphi}{\partial \varphi}-\frac{\overline{v}_\varphi\overline{v}_r-\overline{v}_\theta\overline{v}_\varphi cot\theta}{r}\right)=-\frac{1}{sin\theta}\frac{\partial p}{\partial \varphi}-\left[\frac{1}{r^3}\frac{\partial}{\partial r}\left(r^3\overline{\tau}_{r\varphi}{}^{(v)}\right)+\frac{1}{r sin\theta}\frac{\partial}{\partial \varphi}\left(\overline{\tau}_{\varphi\varphi}^{(v)}\right)+\frac{1}{r sin\theta}\frac{\partial}{\partial \theta}\left(\overline{\tau}_{\theta\varphi}^{(v)} sin\theta\right)+\frac{\overline{\tau}_{\varphi r}^{(v)}-\overline{\tau}_{r\varphi}^{(v)}+\overline{\tau}_{\varphi\theta}^{(v)} cot\theta}{r}\right]$$
$$-\left[\frac{1}{r^3}\frac{\partial}{\partial r}\left(r^3\overline{\tau}_{r\varphi}{}^{(t)}\right)+\frac{1}{r sin\theta}\frac{\partial}{\partial \varphi}\left(\overline{\tau}_{\varphi\varphi}^{(t)}\right)+\frac{1}{r sin\theta}\frac{\partial}{\partial \theta}\left(\overline{\tau}_{\theta\varphi}^{(t)} sin\theta\right)+\frac{\overline{\tau}_{\varphi r}^{(t)}-\overline{\tau}_{r\varphi}^{(t)}+\overline{\tau}_{\varphi\theta}^{(t)} cot\theta}{r}\right]+\overline{\rho} g_\varphi \tag{4}$$

Equations (1)–(4) were solved by using the standard k-ε model as turbulent submodel with standard wall function and considering compressibility effects (Launder and Spalding, 1972). The fluid flow equations were discretized using a finite-volume formulation on the three-dimensional non-uniform unstructured grid (478449 elements) shown previously. The semi-implicit method for pressure-linked equations (SIMPLE) was used to solve the pressure-velocity coupled equations. The spatial discretization of the model equations used first order schemes for convective terms and second order schemes for diffusion terms. First-order time integration was used to discretize temporal derivatives with a time step of $4\bullet10^{-5}$ s. The flow of the solid phase was solved with the Lagrangian formulation using the Discrete Phase Model (DPM).

The momentum balance equation of the DPM reads as follows (Fluent Inc, 2016):

$$\frac{du_p}{dt} = f_D + \frac{g(\rho_p - \rho)}{\rho_p} + f \tag{5}$$

where f_D is the drag force per unit particle mass, function of the Reynolds number according to the following equation

$$f_D = \frac{18\mu}{\rho_p d_p^2}\frac{C_D Re}{24}(u - u_p) \tag{6}$$

The Reynolds number in Equation (6) is defined in the following

$$Re = \frac{\rho d_p |u_p - u|}{\mu} \tag{7}$$

Here, u is the fluid phase velocity, u_p is the particle velocity, μ is the molecular viscosity of the fluid, ρ is the fluid density, ρ_p is the density of the particle, C_D is the drag coefficient and d_p is the particle diameter. Equation (5) incorporates additional forces (f) per unit particle mass. The first of these is the "virtual mass" force, the force required to accelerate the fluid surrounding the particle. This force can be written as:

$$f = \frac{1}{2}\frac{\rho}{\rho_p}\frac{d}{dt}(u - u_p) \tag{8}$$

An additional force arises due to the pressure gradient in the fluid:

$$f = \left(\frac{\rho}{\rho_p}\right)u_p\frac{\partial u}{\partial x} \tag{9}$$

Several laws for drag coefficients, C_D, are available for the Euler-Lagrange Model. The spherical drag law for smooth particles is defined in the following

$$C_D = a_1 + \frac{a_2}{Re} + \frac{a_3}{Re^2} \tag{10}$$

where a_1, a_2 and a_3 are constants given by Morsi and Alexander (1972).

The discrete phase formulation used by Ansys Fluent contains the assumption that the second phase is sufficiently dilute that particle-particle interactions and the effects of the particle volume fraction on the gas phase are negligible. In practice, these requirements imply that the discrete phase must be present at a fairly low volume fraction, usually less than 10–12% (Fluent Inc, 2016). In this work, the dust concentration investigated was equal to 100 g/m^3 with a dust density of 2046 kg/m^3, corresponding to a solid fraction equal to $\alpha = 4.9\bullet10^{-5}$. In these conditions, the momentum transfer from the particles is large enough to alter the turbulence structure while the particle/particle collision may be neglected. This interaction is called two-way coupling according to the classification of Elghobashi (1994).

Fluent predicts the trajectory of a discrete phase particle by integrating the force balance on the particle. Therefore, the DPM uses its own numerical mechanisms and discretization schemes. The unsteady particle tracking integration time step was taken equal to the fluid flow time step. Parallel calculations were performed by means of the segregated pressure-based solver of the code ANSYS Fluent (release 19). In order to achieve convergence, all residuals were set equal to $1\bullet10^{-6}$. For 1 m^3 simulation, the fluid phase was air at constant atmospheric temperature. As initial conditions, we adopted the same conditions used in the standard tests: the container vessel was initially at pressure equal to 21 bar; the connecting tube and the sphere were set to 1 bar. Computations were performed for a dust with density and diameter equal to 2046 kg/m^3 and 250 μm, respectively. The simulation conditions for both standard vessels are summarized in Table 2.

Table 2
Simulation conditions.

	20 L sphere	1 m^3 sphere
Initial pressure of container (bar)	21	21
Initial pressure of sphere and container (bar)	0.4	1
Dust concentration (g/m^3)	100	100
Dust density (kg/m^3)	2046	2046
Dust diameter (μm)	250	250
Time step (s)	$1\bullet10^{-4}$	$4\bullet10^{-5}$
Number of time steps	600	15000

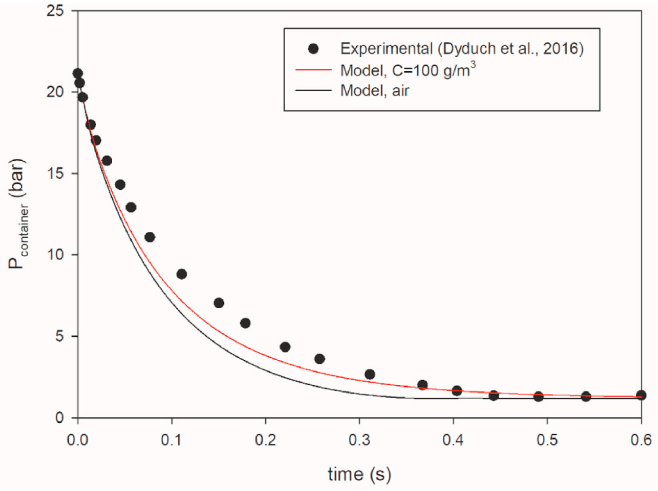

Fig. 4. *Pressure time histories computed in the centre of the dust container for dust free air and dust-air mixture. Literature data are also shown for the sake of comparison* (Dyduch et al., 2016).

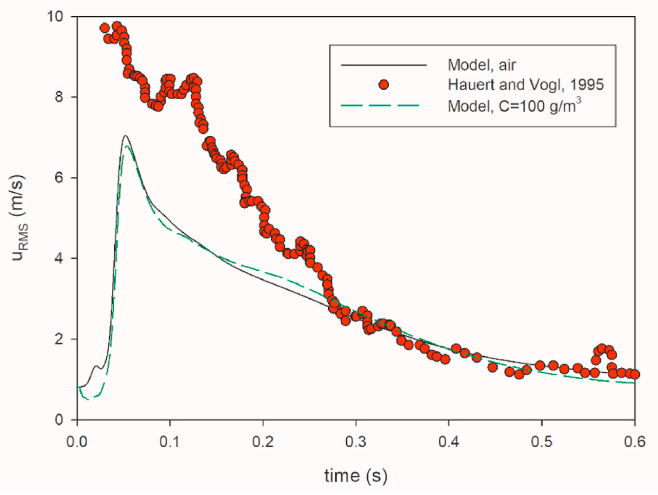

Fig. 5. *RMS turbulence velocity (m/s) as a function of the time at the centre of the 1 m^3 vessel for dust free air and dust-air mixture. Literature data are also shown for comparison* (Hauert and Vogl, 1995).

2.3. 1 m^3 model results

In Fig. 4, the pressure is plotted vs. time as computed in the centre of the dust container. From the pressure trends, the feeding phase during which air or dust-air mixture goes from the container to the sphere may be identified. This phase lasts 0.4 s. Indeed, after 0.4 s, the container pressure reaches 1 bar and the injection of air/dust-air comes to an end. The model results in terms of temporal profile of pressure inside the container are compared to experimental data available in the literature (Dyduch et al., 2016). The comparison shows a very good agreement with a maximum deviation at 0.2 s between the experimental and the theoretical data of the dust/air mixture feeding equal to 20%.

In Fig. 5, the corresponding temporal trend of the root mean square velocity (u_{RMS}) in case of dust-free air and dust at a concentration equal to 100 g/m^3 are shown as computed in the centre of the sphere.

The RMS velocity was calculated from the turbulent kinetic energy by considering an isotropic flow field:

$$k = \frac{3}{2}(u')^2 \tag{11}$$

$$u_{RMS} = \sqrt{\overline{u'^2}} \tag{12}$$

For the sake of comparison, the experimental data measured by Hauert and Vogl (1995) are also shown (Hauert and Vogl, 1995). The experimental data were used only to compare the trend, but a direct comparison is not possible since the geometries of involved vessels are different (spherical in this work while cylindrical in the experimental data) as well as the considered dust (different diameter and density). To avoid a fast soiling on the optical measuring probes in the 1 m^3 cylindrical vessel, Hauert and Vogl (1995) used maize starch (diameter 15 μm, density of about 1000 kg/m^3) concentrations between 30 g/m^3 and 120 g/m^3.

From Fig. 5, it appears that there is a short period of turbulence build up followed by a much longer period of turbulence decay. The turbulence decay starts after few milliseconds from the opening of the valve, well before the end of the injection phase. It is found that the computed u_{RMS} curves are different in the first 300 ms compared to the experimental data, while they show a similar trend after 300 ms, in the turbulence decay phase. Due to the low value of concentration, the flow development in the model is not strongly affected by the dust presence, resulting in overlapped RMS curves in the case of dust-free air and dust with a slight difference in the peak value.

In Fig. 6, the temporal trend of the DPM concentration is shown as computed in the centre of the sphere. For the sake of comparison, the experimental data determined by measuring the light transmission using opto-electronic techniques by Hauert and Vogl (1995) are also shown (Hauert and Vogl, 1995). Hauert and Vogl (1995) used maize starch (diameter 15 μm, density of about 1000 kg/m^3) at 120 g/m^3. Due to the different nature of involved dusts (different diameter and density), a direct comparison is not possible. As for the u_{RMS} trends, it is found that the DPM concentration as computed through the model are different in the first 300 ms compared to the experimental data, while the values fall in the same concentration range after 300 ms.

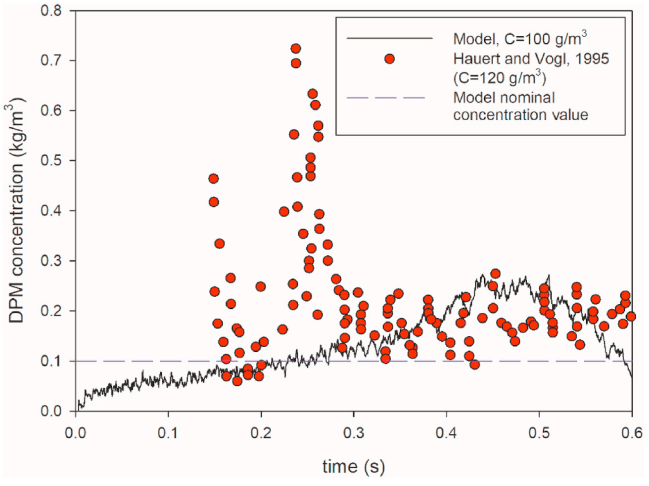

Fig. 6. *DPM concentration (kg/m^3) as a function of the time at the centre of the 1 m^3 vessel. Literature data are also shown for the sake of comparison* (Hauert and Vogl, 1995).

It is worth noting that according to the model simulation, at the ignition delay time (0.6 s) the dust concentration computed at the centre of the sphere is very similar to the nominal value ($C_{nominal}$ = 100 g/m^3).

In Fig. 7 the time sequence of maps of the turbulent kinetic energy is shown as computed over the frontal (x-z) plane in case of dust-free air (a) and dust at 100 g/m^3 (b). It is worth noting that the maps at 400 ms and 600 ms with dust present non-symmetric fields, differently from the results obtained in the case of dust-free air (a). This behaviour has been previously found by Kartushinsky et al. (2011). They developed a three-dimensional RANS numerical method with the appropriate system of closure equations for the transport of gas–solids mixtures. The results showed that the presence of particles in the flow has a significant effect on all the flow variables. Most notably, the distribution of all the parameters becomes asymmetric, because of the gravitational effect on the particles and particle sedimentation (Kartushinsky et al., 2011). Although the level of turbulence is not completely uniform within the sphere, showing a decay moving from the centre to the walls, the variation range of turbulent kinetic energy is very narrow (from 1.25 m^2/s^2 to 0 m^2/s^2).

In Fig. 8 the time sequence of maps of the velocity vectors is shown as computed over the frontal (x-z) plane in case of dust-free air (a) and dust at 100 g/m^3 (b). While the pressure in the dust container falls, the gas velocity significantly decays in time. Fig. 8 also shows that two main vortices are formed at the centre of the sphere, they are well evident at 200 and 400 ms and appear to be almost dissipated at 600 ms. These vortex structures generally result in higher dust concentrations close to the walls and, thus, in regions external to the vortices. Conversely, at the centre of the vortices, the dust concentration is very low. This suggests that the dust is not entrained by the fluid and then the vortices are dead volume for the dust (Di Benedetto et al., 2013; Di Sarli et al., 2015, 2013). In the case of dust dispersion (b), the maximum velocities correspond to the zone of perforated annular nozzle, in particular at the exit of the central hole and of holes in each end cap. In Fig. 9, the area averaged velocity profiles at the exit of the central hole (mid) and of holes in each end cap (z+ and z-) are shown. As the time increases, each profile shows a decay due to the reduction of the pressure gradient from the dust container to the sphere. For each time, the velocity modulus is higher than the value recorded in the centre of the sphere.

The spatial-temporal distribution of dust concentration inside the sphere is represented through the ratio χ between the dust concentration and the nominal dust concentration (C = 100 g/m^3). In Fig. 10, the time sequence of the particle tracks coloured by χ is shown as obtained on the (x-z) plane (a) and in the whole sphere (b) oriented as in the empty image. This figure further confirms that the highest dust concentrations are attained externally to the vortices, whereas the dust concentration is very low inside the vortices. Indeed, the dust is highly concentrated at the sphere walls, reaching concentrations much higher than the nominal value (χ = 2; C = 200 g/m^3), while in the bulk of the sphere, the dust concentration is lower than the nominal value (χ < 1; C < 100 g/m^3). This result is qualitatively in agreement with the findings by Kalejaiye et al. (2010). Lower values of transmission (and then higher values of concentration) were found in correspondence to the probes close to the vessel walls with respect to those closer to the sphere centre. In particular, at each time, an accumulation close to the perforated annular nozzle on the (x-z) plane can be observed. Moreover, starting from 400 ms, the dust creates a three-dimensional cross inside the vessel. In particular, at the ignition time (t = 600 ms), the cloud is not uniform,

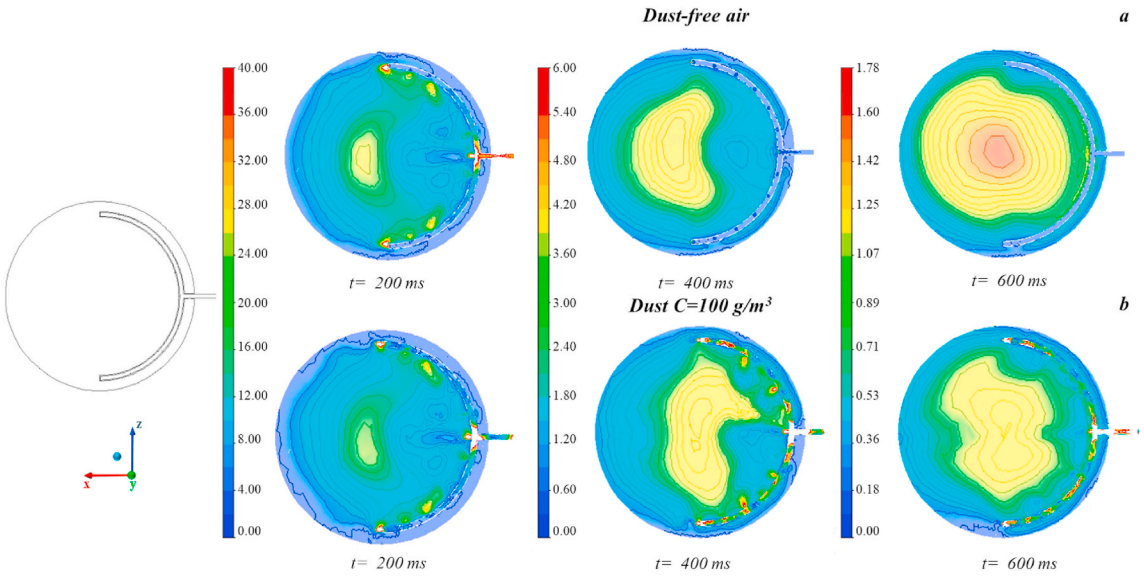

Fig. 7. Time sequence of computed maps of turbulent kinetic energy (m^2/s^2): dust-free air (a) and dust C = 100 g/m^3 (b), (x–z) plane.

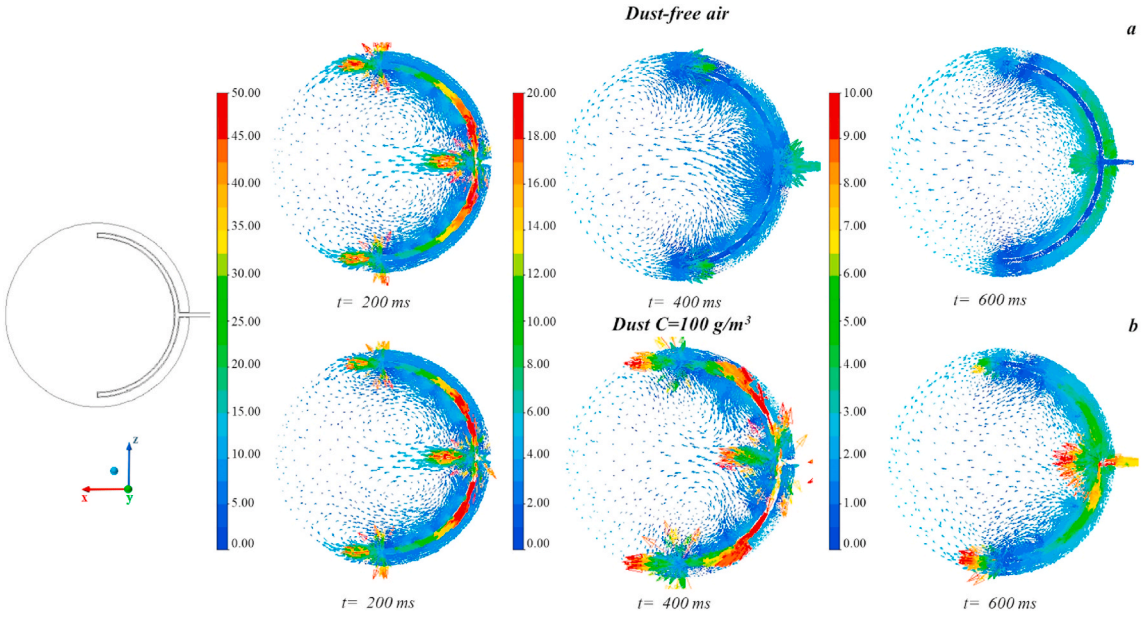

Fig. 8. Time sequence of computed velocity vectors (m/s): dust-free air (a) and dust C = 100 g/m^3 (b), (x–z) plane.

suggesting that the flame will start propagating in a stratified flammable mixture.

3. Comparison between 20 L and 1 m^3 vessels

According to the standard guidelines (ASTM E1226-19, 2019; BS EN 14034-1, 2004; ISO, 1985–1:1985, 1985) and previous results (Bartknecht, 1989; Siwek, 1988, 1977) it is widely accepted that the 20 L and the 1 m^3 vessels would give the same values of the deflagration index, provided that the ignition time are 60 ms and 600 ms, respectively.

In order to give the same value of the deflagration index, the same dust concentration and turbulent kinetic energy should be established inside the vessels.

To verify this, we performed the simulations of the same dust feeding inside the 20 L vessel.

We refer to the dimensionless time τ defined as the ratio between time and ignition delay time (t_d = 60 ms for 20 L vessel; 600 ms for 1 m^3 vessel).

In Fig. 11 the time sequence of the turbulent kinetic energy maps is shown as computed over the frontal (x-y) plane for the 20 L vessel (a) and for the 1 m^3 vessel (b). At all times, the turbulent kinetic energy computed in the 20 L vessel is higher than that found in the 1 m^3 vessel. Notably, the 20 L vessel shows a non-uniform degree of turbulence, resulting in not reliable and not repeatable measurements of the explosibility parameters (Di Benedetto et al., 2013; Di Sarli et al., 2015, 2014, 2013). This issue appears to be solved in the 1 m^3 vessel since the variation range of turbulent kinetic energy from the centre to the wall at the ignition delay time is very narrow (from 1.25 m^2/s^2 to 0 m^2/s^2). However, the values of the turbulent kinetic energy are quite different, even at the ignition delay times (τ = 1).

The spatial-temporal distributions of dust concentration are represented in Fig. 12 through the ratio χ between the dust concentration and the nominal dust concentration (C = 100 g/m^3) as function of the ratio τ computed in the vessel (20 L (a), 1 m^3 (b)). In both the standard vessel,

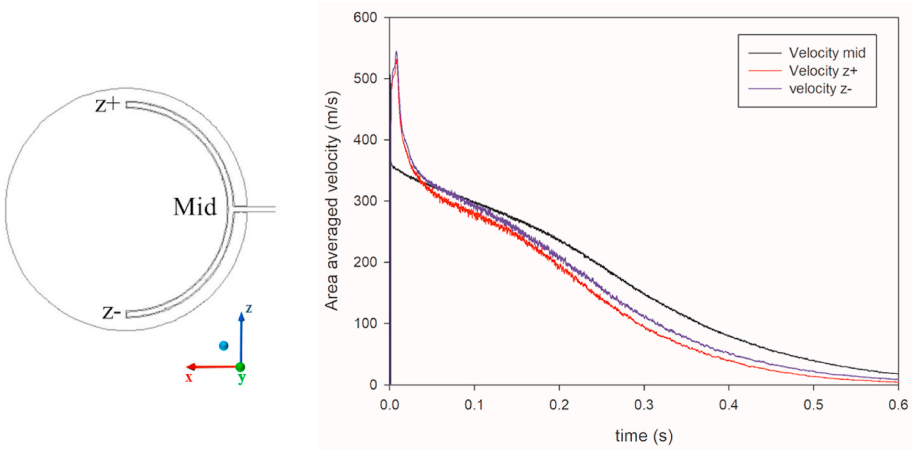

Fig. 9. Area-averaged velocity profiles at the exit of the central hole (mid) and of holes in each end cap (z+ and z-) for dust C = 100 g/m^3 simulation.

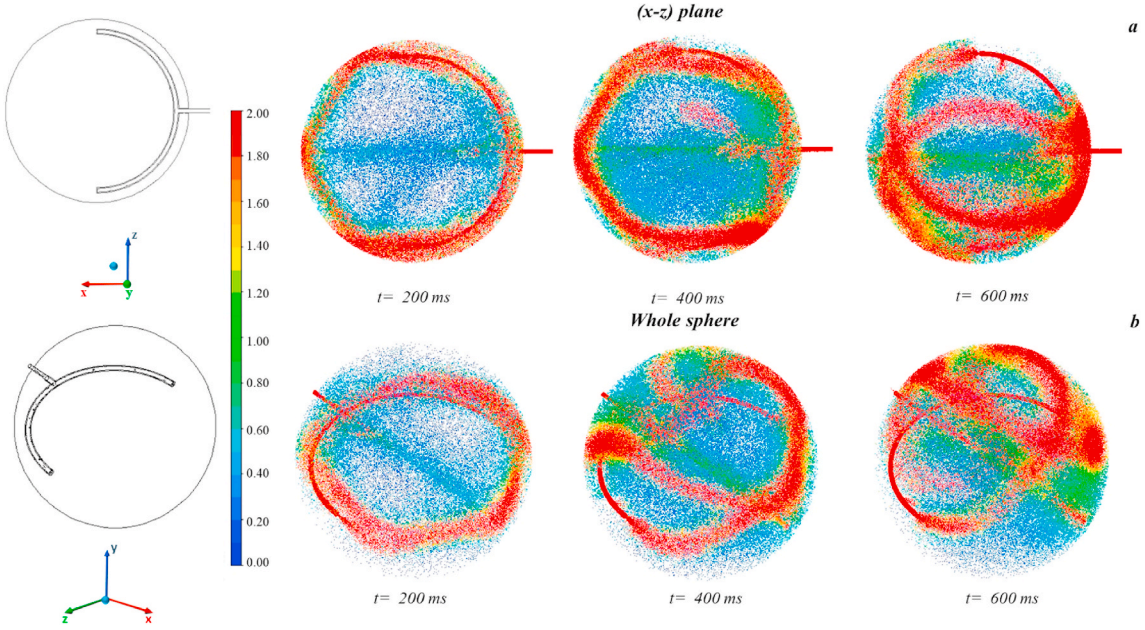

Fig. 10. Time sequence of particle tracks coloured by χ: (x–z) plane (a) and whole sphere (b).

the requirement of a uniform dust cloud within the test volume reported in several standard is not satisfied (ASTM E1226-19, 2019; ASTM E1515-14, 1993; ASTM E2931-13, 2013; BS EN 14034-1, 2004; ISO, 1985–1:1985, 1985) and the dust distribution changes with dust diameter, nominal concentration and shape of the particles. This involves a variability of the results according to the boundary conditions even for the same dust. In particular, the highest dust concentrations are attained externally to the vortices, whereas the dust concentration is very low inside the vortices. Indeed, the dust is highly concentrated at the sphere walls, reaching concentrations much higher than the nominal value (χ = 2; C = 200 g/m^3), while in the bulk of the sphere, the dust concentration is lower than the nominal value ($\chi < 1$; C < 100 g/m^3). In the case of 20 L vessel, dust accumulation in the centre of the sphere can be observed. Moreover, the perforated annular nozzle, used in the 1 m^3 vessel, does not allow the complete feeding of dust within the test volume, as already found in a previous work (Di Sarli et al., 2015).

Fig. 13 shows the temporal trend of the turbulent kinetic energy as computed in the centre of the vessels as a function of the dimensionless time τ. At each time in the ignition point, the vessels show values of turbulent kinetic energy very different from each other. In particular, at the ignition delay time ($\tau = 1$), the turbulent kinetic energy in the 20 L vessel is still high (42.30 m^2/s^2) and very different from that in 1 m^3 vessel (1.24 m^2/s^2). It suggests that after 60 ms the degree of turbulence within the 20 L sphere is not uniform and not comparable to that found in the 1 m^3 vessel. This does not satisfy the necessary requirement of comparable level of turbulence at the moment of ignition in the two vessels reported in the standards and in the calibration procedures.

Fig. 14 shows the temporal trend of the DPM concentration as computed in the centre of the vessels as a function of the dimensionless time τ. At ignition, the vessels show DPM concentration values very different from each other. In particular, in the 20 L vessel the dust concentration is higher than that found in the 1 m^3 vessel. At the ignition delay time ($\tau = 1$), the DPM concentration in the 20 L vessel is still high (C = 990 g/m^3) and very different from the nominal value (C = 100 g/m^3) and from that in 1 m^3 vessel (C = 70 g/m^3). The highest values of turbulent kinetic energy and dust concentration at the ignition delay time in the centre of the 20 L sphere (where ignition occurs) may explain the frequent overdriving leading to false positives in smaller explosion chambers, mostly in the case of weakly reactive and organic dusts (Proust et al., 2007).

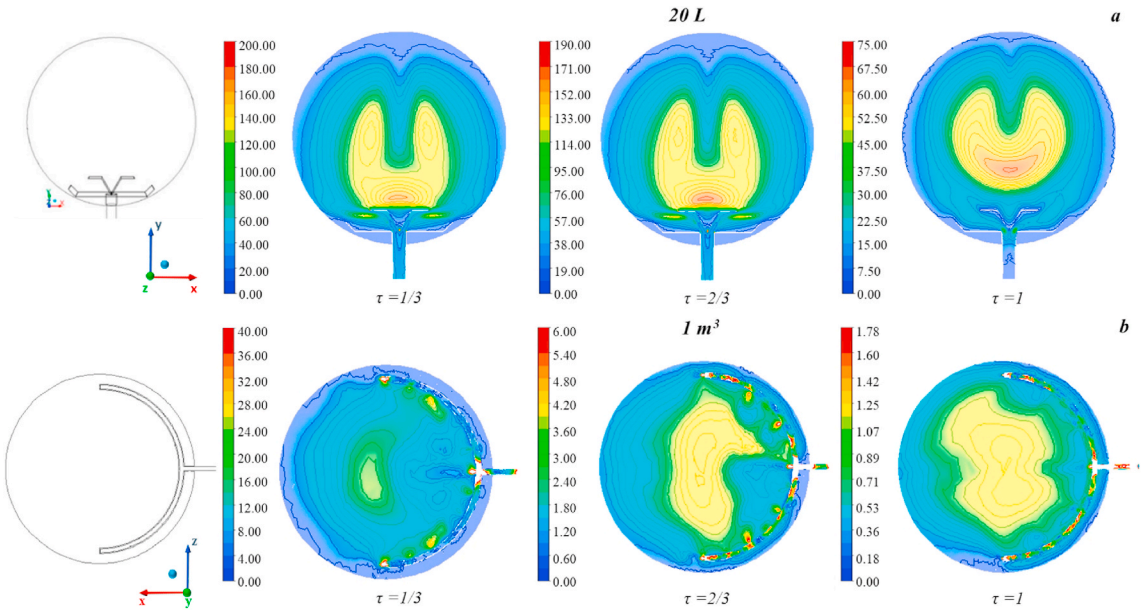

Fig. 11. Computed maps of turbulent kinetic energy (m2/s2) as function of the ratio τ: 20 L sphere (a) ((x–y) plane) and 1 m^3 vessel (b), (x–z) plane.

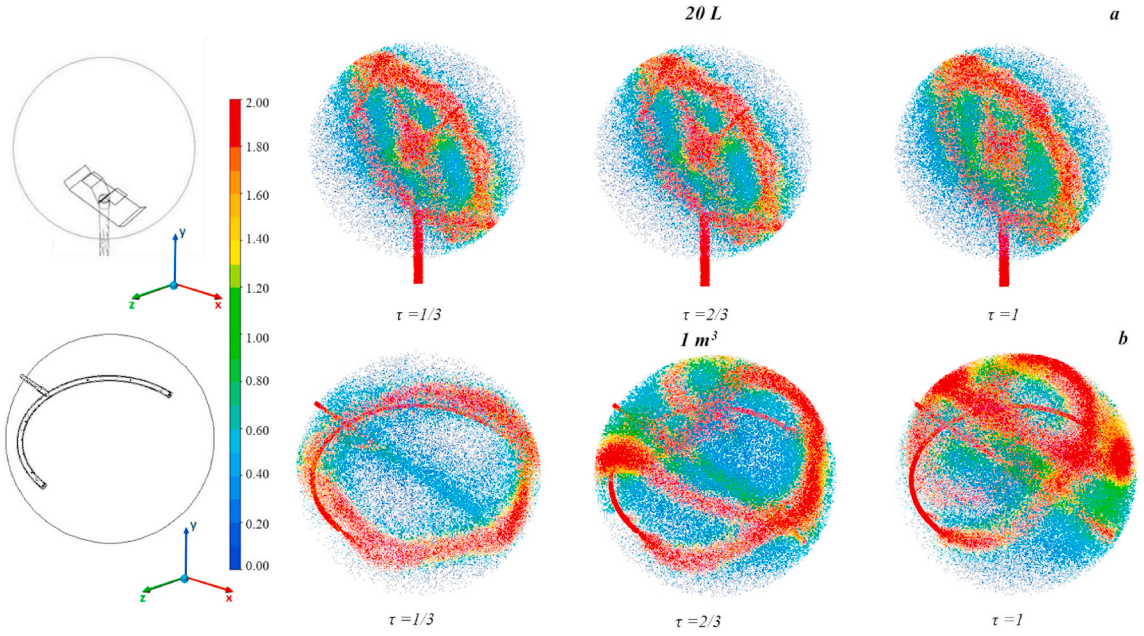

Fig. 12. Particle tracks coloured by χ as function of the ratio τ computed in the whole spheres: 20 L sphere (a) and 1 m^3 vessel (b).

To assess the effect of turbulence on the evaluation of deflagration index with the two standard vessels, we estimated the theoretical K_{St} through the thin-flame model by Dahoe et al. (1996). In this model, the content of the vessels consists of a spherical inner region of completely burnt material, encapsulated by an outer region of completely unburnt mixture. The model assumes that the laminar burning velocity S_l remains constant during the explosion (i.e. it does not depend on the dust concentration). As concern the maximum rate of pressure rise $\left(\frac{dP}{dt}\right)_{MAX}$ to be included in the formula of Lewis von Elbe (Eq. (13)), it was computed maximizing the equation by Dahoe et al. (1996), which link the pressure P and the turbulent burning velocity S_t to the rate of pressure rise (Eq. (14)). The evaluation of the turbulent burning velocity as function of the turbulent fluctuations (u') was performed through Equation (15) by Pocheau (1994).

The equations used are in the following:

$$K_{St} = \left(\frac{dP}{dt}\right)_{MAX} \left(\frac{4}{3}\pi R_{vessel}^3\right)^{\frac{1}{3}} \tag{13}$$

$$\frac{dP}{dt} = 3\frac{P_{MAX} - P_0}{R_{vessel}} \left[1 - \left(\frac{P_0}{P}\right)^{\frac{1}{\gamma}} \frac{P_{MAX} - P}{P_{MAX} - P_0}\right]^{\frac{2}{3}} \left(\frac{P}{P_0}\right)^{\frac{1}{\gamma}} S_t \tag{14}$$

$$S_t = S_l \cdot \left(1 + \left(\frac{u'}{S_l}\right)^2\right)^{0.5} \tag{15}$$

P_{max} is the maximum pressure reached in a closed vessel (set at 8 bar); P_0 is the initial pressure (assumed equal to 1 bar); R_{vessel} is the radius of the spherical vessel.

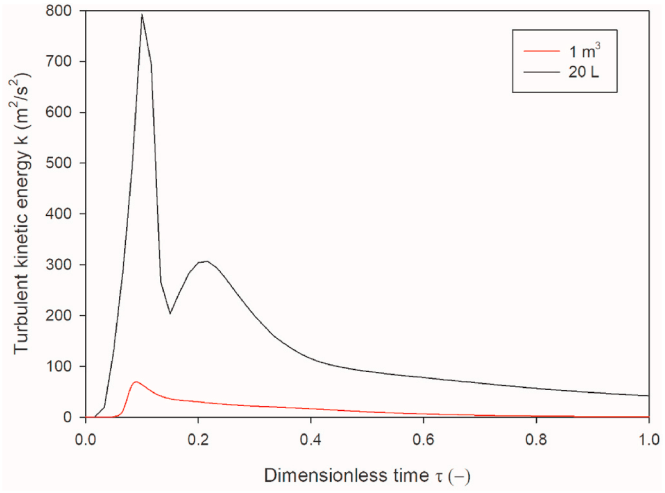

Fig. 13. Temporal trends of turbulent kinetic energy (m^2/s^2) as computed in the centre of the vessels for 20 L sphere and 1 m^3 vessel as a function of the dimensionless time τ

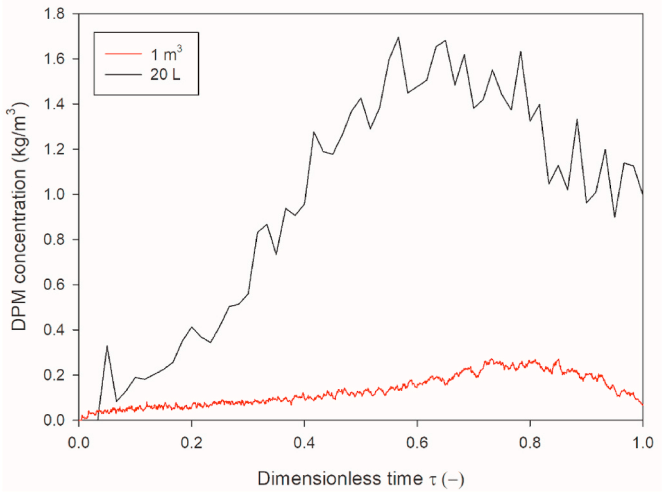

Fig. 14. DPM concentration as computed in the centre of the spheres for 20 L sphere and 1 m^3 vessel as a function of the dimensionless time τ

The results and the differences between the two vessels are summarized in Table 3. In the case of the 1 m^3 vessel, a controlled turbulence level is realized. Conversely, in the case of 20 L sphere, a non-uniform spatial distribution is found. The propagating flame will encounter zones with concentration much higher than the nominal value ($\chi > 1$) and zones with concentration much lower than the nominal value ($\chi < 1$). It was found that the K_{St} estimated in the 20 L vessel is 2.4 times higher than the value obtained in the 1 m^3 vessel.

Therefore, turbulence level has a crucial role on the K_{St} assessment. The turbulence intensity seems weak and more or less the same in the 1 m^3 vessel at the delay time, whereas it may vary significantly in the 20 L sphere. If the Kst depended solely on the level of turbulence, the assessment within the 20 L vessel would always be more conservative than that in the 1 m^3 vessel. Conversely, other effects must be taken into consideration such as overdriving, preheating and thermal radiation (Clouthier et al., 2019; Going et al., 2000; Proust et al., 2007; Taveau et al., 2019).

When performing explosion/flammability tests by using chemical igniters (according to the standard procedure), the flame is overdriven by the igniters explosion and mainly controlled by them. Conversely, the effects of preheating, thermal radiation and turbulence level on the explosion parameters are not foreseeable as they strongly depend on the type of investigated dust. For this reason, the calibration cannot be generalizable to all types of dust but each one needs its own calibration to assess the relative turbulence level. However, the *ad hoc* calibration procedure would lead to the drop of the idea of a standardized procedure suitable for all the dusts.

The obtained results in the investigated case suggest that, whatever the volume of testing vessels, different explosion vessel configuration and dispersion method have to be developed to perform a correct and reliable evaluation of the flammability and explosibility parameters for dusts and dust mixtures.

4. Conclusions

CFD simulations allow the quantification of the temporal/spatial profiles of turbulent kinetic energy and dust concentration in the 1 m^3 vessel. Comparison of the computed turbulent kinetic energy and dust concentration with the (few) experimental data available show a good agreement only at times higher than 300 ms. The spatial distribution of the turbulent kinetic energy is quite uniform inside the whole vessel. Conversely, the dust is mainly concentrated at the outer zones of the vortices generated in the vessel and then dust concentration is not uniform. Simulations also show that a large part of dust is not fed, being trapped in the annular nozzle. Comparison with the turbulent kinetic energy in the 20 L vessel, shows that the turbulence level in the 20 L is much higher. As a result, the deflagration index estimated in the lab-scale 20 L vessel, considering the spatial distribution of the level of turbulence (calculated through CFD simulations), was found to be 2.4 times higher than the value obtained in the 1 m^3 vessel, providing a more conservative assessment. It is worth noting other effects must be taken into consideration in the K_{St} assessment such as overdriving, preheating, thermal radiation and turbulence level.

CRediT authorship contribution statement

Maria Portarapillo: Methodology, Investigation, Writing - original draft, Writing - review & editing. **Marco Trofa:** Methodology, Writing - review & editing. **Roberto Sanchirico:** Writing - review & editing. **Almerinda Di Benedetto:** Conceptualization, Writing - original draft, Writing - review & editing, Supervision.

Declaration of competing interest

The authors declare that they have no known competing financial interests or personal relationships that could have appeared to influence the work reported in this paper.

Table 3
Comparison between the 20 L and 1 m^3 vessels.

	20 L sphere	1 m^3 sphere
Turbulence level and control	High turbulence level, not uniform in space	Low turbulence level, uniform in space
Turbulent kinetic energy in the centre (m^2/s^2) at $\tau = 1$	42.30	1.24
Dust concentration distribution	Not well mixed, low level of uniformity	Not well mixed, low level of uniformity
Dust concentration at the centre (g/m^3) at $\tau = 1$	990	70
Theoretical deflagration index (bar m/s)	92.40	37.80
K_{St} (20 L)/K_{St} (1m^3)	2.4	

References

ASTM E1226-19, 2019. Standard Test Method for Explosibility of Dust Clouds. PA. ASTM Int. West Conshohocken, pp. 1–15. https://doi.org/10.1520/E1226-19.

ASTM E1515-14, 1993. Standard Test Method for Minimum Explosible Concentration of Combustible Dusts 1. PA. ASTM Int. West Conshohocken, pp. 1–9. https://doi.org/10.1520/E1515-14.

ASTM E2931-13, 2013. Standard Test Method for Limiting Oxygen (Oxidant) Concentration of Combustible. PA. ASTM Int. West Conshohocken, pp. 1–9. https://doi.org/10.1520/E2931-13.

Bartknecht, W., 1989. Dust Explosions: Course, Prevention, Protection. Springer Verlag.

BS EN 14034-1, 2004. Determination of Explosion Characteristics of Dust Clouds Part 1: Determination of Maximum Pressure Pmax of Dust Clouds 3.

Cashdollar, K.L., 1996. Coal dust explosibility. J. Loss Prev. Process. Ind. 9, 65–76. https://doi.org/10.1016/0950-4230(95)00050-X.

Cashdollar, K.L., Chatrathi, K., 1992. Minimum explosible dust concentrations measured in 20-L and 1-M3 chambers. Combust. Sci. Technol. 87, 157–171. https://doi.org/10.1080/00102209208947213.

Clouthier, M.P., Taveau, J.R., Dastidar, A.G., Morrison, L.S., Zalosh, R.G., Ripley, R.C., Khan, F.I., Amyotte, P.R., 2019. Iron and aluminum powder explosibility in 20-L and 1-m3 chambers. J. Loss Prev. Process. Ind. 62, 103927. https://doi.org/10.1016/J.JLP.2019.103927.

Dahoe, A.E., Cant, R.S., Scarlett, B., 2002. On the decay of turbulence in the 20-liter explosion sphere. Flow, Turbul. Combust. 67, 159–184. https://doi.org/10.1023/A:1015099110942.

Dahoe, A.E., Zevenbergen, J.F., Lemkowitz, S.M., Scarlett, B., 1996. Dust explosions in spherical vessels: the role of flame thickness in the validity of the “cube-root law. J. Loss Prev. Process. Ind. 9, 33–44. https://doi.org/10.1016/0950-4230(95)00054-2.

Di Benedetto, A., Garcia-Agreda, A., Russo, P., Sanchirico, R., 2012. Combined effect of ignition energy and initial turbulence on the explosion behavior of lean gas/dust-air mixtures. Ind. Eng. Chem. Res. 51, 7663–7670. https://doi.org/10.1021/ie201664a.

Di Benedetto, A., Russo, P., Amyotte, P., Marchand, N., 2010. Modelling the effect of particle size on dust explosions. Chem. Eng. Sci. 65, 772–779. https://doi.org/10.1016/j.ces.2009.09.029.

Di Benedetto, A., Russo, P., Sanchirico, R., Di Sarli, V., 2013. CFD simulations of turbulent fluid flow and dust dispersion in the 20 liter explosion vessel. AIChE 59, 2485–2496. https://doi.org/10.1002/aic.

Di Sarli, V., Russo, P., Sanchirico, R., Di Benedetto, A., 2014. CFD simulations of dust dispersion in the 20 L vessel: effect of nominal dust concentration. J. Loss Prev. Process. Ind. 27, 8–12. https://doi.org/10.1016/j.jlp.2013.10.015.

Di Sarli, V., Russo, P., Sanchirico, R., Di Benedetto, A., 2013. CFD simulations of the effect of dust diameter on the dispersion in the 20L bomb. Chem. Eng. Trans. 31, 727–732.

Di Sarli, V., Sanchirico, R., Russo, P., Di Benedetto, A., 2015. CFD modeling and simulation of turbulent fluid flow and dust dispersion in the 20-L explosion vessel equipped with the perforated annular nozzle. J. Loss Prev. Process. Ind. 38, 204–213. https://doi.org/10.1016/j.jlp.2015.09.015.

Dust Safety Science, 2020. Combustible Dust Incident Database.

Dyduch, Z., Toman, A., Adamus, W., 2016. Measurements of turbulence intensity in the standard 1 m3 vessel. J. Loss Prev. Process. Ind. 40, 180–187. https://doi.org/10.1016/j.jlp.2015.12.019.

Elghobashi, S., 1994. On predicting particle-laden turbulent flows. Appl. Sci. Res. 52, 309–329. https://doi.org/10.1007/BF00936835.

Fluent Inc, 2016. Discrete phase modelling. ANSYS FLUENT User’s Guid, pp. 1–170.

Going, J.E., Chatrathi, K., Cashdollar, K.L., 2000. Flammability limit measurements for dusts in 20-L and 1-m3 vessels. J. Loss Prev. Process. Ind. 13, 209–219. https://doi.org/10.1016/S0950-4230(99)00043-1.

Hauert, F., Vogl, A., 1995. Measurement of Dust Cloud Characteristics in Industrial Plants (Number: PL 910695).

ISO 6184-1:1985, 1985. Explosion Protection Systems, Part 1, Determination of Explosion Indices of Combustible Dusts in Air.

Kalejaiye, O., 2001. An Investigation of the Effectiveness of Dust Dispersion in the Siwek 20-l Chamber. Dalhousie University, Halifax, Nova Scotia.

Kalejaiye, O., Amyotte, P.R., Pegg, M.J., Cashdollar, K.L., 2010. Effectiveness of dust dispersion in the 20-L Siwek chamber. J. Loss Prev. Process. Ind. 23, 46–59. https://doi.org/10.1016/j.jlp.2009.05.008.

Kartushinsky, A.I., Michaelides, E.E., Rudi, Y.A., Tisler, S.V., Shcheglov, I.N., 2011. Numerical simulation of three-dimensional gas-solid particle flow in a horizontal pipe. AIChE J. 57, 2977–2988. https://doi.org/10.1002/aic.12528.

Launder, B.E., Spalding, D.B., 1972. Lectures in Mathematical Models of Turbulence. Academic Press, London; New York.

Morsi, S.A., Alexander, A.J., 1972. An investigation of particle trajectories in two-phase flow systems. J. Fluid Mech. 55, 193–208. https://doi.org/10.1017/S0022112072001806.

NFPA, N.68, 2018. Explosion Protection by Deflagration Venting.

Pocheau, A., 1994. Scale invariance in turbulent front propagation. Phys. Rev. E 49, 1109–1122. https://doi.org/10.1103/PhysRevE.49.1109.

Portarapillo, M., Di Sarli, V., Sanchirico, R., Di Benedetto, A., 2020. CFD simulation of the dispersion of binary dust mixtures in the 20 L vessel. J. Loss Prev. Process. Ind. https://doi.org/10.1016/j.jlp.2020.104231.

Proust, C., Accorsi, A., Dupont, L., 2007. Measuring the violence of dust explosions with the “20 l sphere” and with the standard “ISO 1 m3 vessel”. Systematic comparison and analysis of the discrepancies. J. Loss Prev. Process. Ind. 20, 599–606. https://doi.org/10.1016/j.jlp.2007.04.032.

Pu, Y.K., Jarosinski, J., Johnson, V.G., Kauffman, C.W., 1991. Turbulence effects on dust explosions in the 20-liter spherical vessel. Symp. Combust. 23, 843–849. https://doi.org/10.1016/S0082-0784(06)80338-3.

Rodgers, S.A., Ural, E.A., 2011. Practical issues with marginally explosible dusts—evaluating the real hazard. Process Saf. Prog. 30, 266–279. https://doi.org/10.1002/prs.

Russo, P., Amyotte, P.R., Khan, F.I., Di Benedetto, A., 2013. Modelling of the effect of size on flocculent dust explosions. J. Loss Prev. Process. Ind. 26, 1634–1638. https://doi.org/10.1016/j.jlp.2013.07.012.

Russo, P., Di Benedetto, A., 2013. Review of a dust explosion modeling. Chem. Eng. Trans. 31, 955–960. https://doi.org/10.3303/CET1331160.

Siwek, R., 1988. Reliable determination of the safety characteristics in 20-l apparatus. Proceedings of the Flammable Dust Explosion Conference, pp. 529–573.

Siwek, R., 1977. 20-l-Laborapparatur Fur die Bestimmung der Explosionskenngrossen brennbarer Staube. [20-liter laboratory apparatus for determination of explosion characteristics of combustible dusts]. Ciba-Geigy AG(Basel) and Winterthur Engineering College, Winterthur, Switzerland.

Taveau, J.R., Lemkowitz, S.M., Hochgreb, S., Roekaerts, D., 2018. Scaling up metal dusts deflagrations severity. In: Proceedings of the Twelfth International Symposium on Hazards, Prevention, and Mitigation of Industrial Explosions. Soesterberg, Netherlands.

Taveau, J.R., Lemkowitz, S.M., Hochgreb, S., Roekaerts, D.J.E.M., 2019. Metal dusts explosion hazards and protection. Chem. Eng. Trans. 77, 7–12. https://doi.org/10.3303/CET1977002.

van der Wel, P.G.J., van Veen, J.P.W., Lemkowitz, S.M., Scarlett, B., van Wingerden, C.J. M., 1992. An interpretation of dust explosion phenomena on the basis of time scales. Powder Technol. 71, 207–215. https://doi.org/10.1016/0032-5910(92)80010-T.

Zhen, G., Leuckel, W., 1996. Determination of dust-dispersion-lnduced turbulence and its influence on dust explosions. Combust. Sci. Technol. 113, 629–639. https://doi.org/10.1080/00102209608935518.